Sains Malaysiana 54(1)(2025): 291-302
http://doi.org/10.17576/jsm-2025-5401-23

Performance of Graphene Oxide-Supported Co_3O_4 with Assisted Urea as Electrocatalysts for Oxygen Reduction Reaction in PEMFCs

(Prestasi Grafin Oksida Tersokong Co_3O_4 dengan Terbantu Urea sebagai Elektromangkin bagi Tindak Balas Penurunan Oksigen dalam PEMFC)

NUR UBAIDAH SAIDIN[1,3], NURUL NORAMELYA ZULKEFLI[1], NOR EZZATI AMIRA MUSTAPA PADZIR[2], NURAZILA MAT ZALI[3], THYE FOO CHOO[3], ROZAN MOHAMAD YUNUS[1] & MOHD SHAHBUDIN MASDAR[1,2,*]

[1]Fuel Cell Institute, Universiti Kebangsaan Malaysia, 43600 UKM Bangi, Selangor, Malaysia
[2]Department of Chemical & Process Engineering, Faculty of Engineering & Built Environment, Universiti Kebangsaan Malaysia, 43600 UKM Bangi, Selangor, Malaysia
[3]Malaysian Nuclear Agency, Bangi, 43000 Kajang, Selangor, Malaysia

Received: 21 June 2024/Accepted: 4 November 2024

ABSTRACT

In this work, cobalt oxide (Co_3O_4) nanoparticles supported on a graphene oxide (GO) electrocatalyst were synthesized using a simple and low-cost hydrothermal route for oxygen reduction reaction (ORR) in fuel cells. The effects of varying the urea concentration on the physicochemical and electrochemical characteristics were investigated in alkaline media using field emission scanning electron microscope (FESEM), X-ray diffraction (XRD), Raman spectroscopy, cyclic voltammetry (CV), linear sweep voltammetry (LSV), and chronoamperometry. The electrocatalyst prepared using cobalt acetate tetrahydrate and urea with a molar ratio of 1:1 exhibited the best ORR activity where the highest onset potential (E_{onset}) at 0.88 V through four-electron mechanism at 25 °C. The synthesized electrocatalyst also showed improved stability compared with Pt/C. Although CN1-1 exhibits a lower power density (37.9 mW cm^{-2}) compared to Pt/C (173.6 mW cm^{-2}), it is still expected to be suitable as an ORR electrocatalyst for proton exchange membrane fuel cells (PEMFCs).

Keywords: Electrocatalyst; fuel cell; graphene oxide; hydrothermal; oxygen reduction reaction

ABSTRAK

Dalam kajian ini, kobalt dioksida (Co_3O_4) berbentuk zarah nano yang disokong grafin oksida (GO) disintesis menggunakan kaedah hidroterma yang mudah dan berkos rendah. Bahan ini digunakan sebagai elektromangkin untuk tindak balas penurunan oksigen (ORR) dalam sel fuel. Kesan perubahan kandungan urea terhadap sifat fiziko-kimia serta elektrokimia dikaji dalam medium alkali menggunakan mikroskop pengimbas elektron pancaran medan (FESEM), pembelauan sinar-X (XRD), spektroskopi Raman, voltametri kitaran (CV), sapuan voltametri linear (LSV) dan kronoamperometri. Elektromangkin yang disediakan menggunakan kobalt asetat tetrahidrat dan urea dengan nisbah 1:1 menunjukkan aktiviti ORR terbaik dengan potensi permulaan (E_{onset}) pada 0.88 V melalui mekanisme empat elektron pada 25 °C. Ia juga menunjukkan kestabilan yang lebih baik berbanding Pt/C. Walaupun CN1-1 mempunyai ketumpatan kuasa 37.9 mW cm^{-2} yang lebih rendah berbanding Pt/C (173.6 mW cm^{-2}), ia dijangka masih sesuai digunakan sebagai elektromangkin ORR dalam aplikasi sel fuel membran penukaran proton (PEMFC).

Kata kunci: Elektromangkin; grafin oksida; hidroterma; sel fuel; tindak balas penurunan oksigen

INTRODUCTION

The advancement in science and technology have improved the quality of human life, but they also led to a higher energy requirement for portable electronic devices, industries, household purposes, aerospace, and electric vehicle applications. Conventional fossil fuels effectively satisfy the global energy demands, but their reserves are diminishing rapidly. Moreover, the utilization of fossil fuels has given rise to concerns about a range of ecological issues, encompassing air pollution, oil leakage, climate change, and acid rain, all of which pose threats to human well-being and contribute to the escalation of global warming induced by carbon dioxide (CO_2) emission (Basri et al. 2020; Wan Mansor et al. 2020). These challenges have spurred investigations into the development of eco-friendly, efficient, and durable energy conversion and storage devices, such as rechargeable lithium-ion batteries, metal–air batteries, fuel cells, and supercapacitors. These devices are being explored as alternative energy sources for rapidly expanding portable electronic devices and

next-generation hybrid electric vehicles (Olabi et al. 2021; Zakaria, Kamarudin & Wahid 2021). Hydrogen fuel cells have attracted significant research attention for energy conversion due to their user-friendly nature, high theoretical energy densities, adequate energy conversion efficiency, and minimal to nonexistent pollutant emissions (Tashie-Lewis & Nnabuife 2021; Yusoff & Suresh 2021).

The primary obstacle for hydrogen fuel cells lies in developing electrocatalysts, particularly the oxygen reduction reaction (ORR), which exhibits sluggish reaction kinetics (Chandrasekaran et al. 2020; Sun, Alonso & Bian 2021). The main objective and obstacle in fuel cell technologies is the development of efficient electrocatalysts (Rahman et al. 2021; Tellez-Cruz et al. 2021). Sluggish and intricate ORRs require a substantial amount of electrocatalysts to expedite the reaction, consequently augmenting the manufacturing cost of fuel cell devices (Saidin et al. 2023).

Precious metals, such as platinum (Pt) and palladium (Pd), have proven to be efficient electrocatalysts for the ORR. However, their utilization in large-scale practical applications is hindered by their exorbitant cost, limited availability, and inadequate stability. Consequently, many scientists have focused their efforts on developing the most prevalent oxides of 3d transition metals (Mn, Fe, Co, Ni, Cu) as electrocatalysts for ORR. These electrocatalysts come in different structures (such as spinel and perovskite) and morphologies (including spheres, rods, wires, fibers, flakes, and sheets). Previous research focused on ORR activity during electrochemical performance testing in terms of structure, particle size, and morphological effects (Kaewsai et al. 2018; Ye et al. 2020). Spinel-structured cobalt-based transition metal oxides, such as cobalt (II, III) oxide (Co_3O_4), have been employed as non-precious electrocatalysts due to their varied valence states, low cost, and structural stability, which allow for significant fine-tuning of their electrocatalytic characteristics (Shahid et al. 2020; Yang et al. 2019b). Nevertheless, the electrochemical capabilities of unmodified transition metal oxides remain constrained due to various challenges, including inadequate electrical conductivity, limited surface-active sites, subpar charge transfer ability, restricted surface area, and unmanageable dispersion of Co_3O_4 (Gebremariam et al. 2018).

Carbon-based materials, such as graphene (Choi, Ashok Kumar & Baek 2015; Wang, Zhu & Chen 2018), carbon black (Ji et al. 2021; Yang et al. 2019a), carbon nanotubes (Roudbari, Ojani & Raoof 2020; Zhao et al. 2019), and porous carbon (Khan et al. 2016; Zhu et al. 2020), have been employed to enhanced the electron transfer capacity, surface area, ion/electron diffusion paths, charge transfer ability, and dispersion of Co_3O_4. Reduced graphene oxide (rGO) is a widely recognized form of carbon that consists of a single layer of sp^2-hybridized carbon atoms arranged in a hexagonal lattice. It possesses various distinctive characteristics, including a large surface area, high electrical conductivity, good thermal and chemical stability, excellent mechanical property, and efficient pathways for electron transport. rGO is a highly advantageous material for developing various hybrid electrocatalysts using electrochemical energy conversion and storage devices, thanks to its attractive features.

Graphene-supported hybrid electrocatalysts, consisting of both precious and non-precious materials, have been developed by several synthesis methods in recent studies. These electrocatalysts have been thoroughly assessed for their electrochemical performance. Co_3O_4 experiences detachment from the support over time due to the direct application of Co_3O_4 onto the carbonaceous support (Sun et al. 2020). A novel synthesis method must be devised to regulate the separation of Co_3O_4 from the substrate. Sun et al. (2020) employed urea to develop a carbonaceous support with a porous structure. The process of urea polymerization resulted in the creation of a structure that had a hierarchical arrangement of pores, with Co_3O_4 evenly dispersed on the carbon-based support. The material developed demonstrated exceptional catalytic efficacy and durability due to its porous configuration and plentiful oxygen vacancies in Co_3O_4. Nevertheless, this study did not provide information regarding the impact of various urea compositions on the performance of the ORR. Osaimany et al. (2019) produced spinel $NiCo_2O_4$ micro-shrubs and rGO-supported hybrid electrocatalysts by modifying the initial metal precursors. This was achieved by employing various compositions of urea, nickel, and cobalt as the precursors. The electrocatalyst with a lower mass loading demonstrated superior ORR activity, characterized by a higher onset potential (0.82 V), a greater diffusion limiting current density (2.06 mA cm^{-2}), and a faster reaction rate (62 mV dec^{-1}) through a four-electron transfer mechanism (n=3.91. While several studies have investigated using urea as a carbon source for a variety of applications (He et al. 2022; Lai et al. 2020), there has been little research on the specific impact of urea addition on ORR electrocatalytic activity of Co_3O_4.

In this work, the synthesis of Co_3O_4 nanoparticles supported on graphene oxide (GO) electrocatalysts was achieved by a hydrothermal method, with the concentration of urea in the reaction system being systematically adjusted to control the process. Urea was employed to generate a porous architecture and serve as a reducing agent to enhance the generated material's performance as an electrocatalysts for ORR. An investigation was conducted to examine the impact of varying concentrations of urea on the physicochemical and electrochemical properties of the material. The electrocatalyst, which was produced using cobalt acetate tetrahydrate and urea in a 1:1 molar ratio, had the highest activity for the ORR. The electrocatalyst exhibited an onset potential of 0.88 V and a limiting current density of 4.49 mA cm^{-2} for the ORR. These measurements were obtained at room temperature in 0.1 M KOH solution, and the ORR proceeded through a four-electron

mechanism. Subsequently, the performance of synthesized electrocatalyst in a single fuel cell PEMFC was evaluated, resulting in a power density of 37.9 mW cm^{-2} at 60 °C and superior stability compared to Pt/C.

MATERIALS AND METHODS

MATERIALS AND CHEMICALS

The following chemicals were obtained from Sigma-Aldrich: cobalt acetate tetrahydrate [$Co(CH_3COO)_2.4H_2O$)], urea [$CO(NH_2)_2$], GO, and Nafion (5 wt. %). The potassium hydroxide (KOH) was acquired from Scharlau. The chemicals employed were analytical grade and utilized without any modifications. The experiment used deionized water as the solvent.

SYNTHESIS OF Co_3O_4/GO

At first, solutions of $Co(CH_3COO)_2.4H_2O$ (0.01 M) and $CO(NH_2)_2$ with different molarities were produced using deionized water. The molar ratios of $Co(CH_3COO)_2.4H_2O$ to $CO(NH_2)_2$ were set at 2:1, 1:1, and 1:2. A GO (1 mg mL^{-2}) was evenly dispersed in the solutions using ultrasonic (30 min), and then purged with N_2 gas to remove any other gas. The solutions were transferred into a 50 mL autoclave made of stainless steel and lined with Teflon. The autoclave was sealed and maintained at the temperature of 200 °C for a duration of 6 h. Once the temperature reached ambient level, the resulting substances were gathered using filtration. They were then rinsed many times with deionized water and ethanol to eliminate any surplus reagent. Finally, the substances were left to dry at 25 °C overnight. Subsequently, the dried powders that were prepared were subjected to calcination in the tube furnace (Nabertherm) in an argon atmosphere at a temperature of 200 °C for a duration of 3 h. The fluffy black substances gathered once they had cooled down to the ambient temperature. The samples were then designed as CNx (CN2-1, CN1-1, and CN1-2) based on the molar ratios of $Co(CH_3COO)_2.4H_2O$ to $CO(NH_2)_2$, which were 2:1, 1:1, and 1:2, respectively. In addition, CN0 was obtained using the identical method, however without the use of $CO(NH_2)_2$. Figure 1 depicts the synthesis process.

PHYSICOCHEMICAL CHARACTERIZATION

The crystallographic characteristics of the electrocatalysts were analyzed using X-ray diffraction (XRD) in reflection mode. The XRD measurements were performed with Cu kα radiation at a wavelength of 0.15406 nm, an acceleration voltage of 40 kV, and a scanning rate of 2° min^{-1}. The scanning was from 10° to 80° on PANalytical X'Pert PRO MPD PW 3040/60. The Raman spectra of all produced samples were obtained using Raman spectrometer (Renishaw, InVia Reflex) equipped with a 532 nm argon ion laser source. These spectra were used to access the level of graphitization, carbon atom disorder, and surface defects. The surface morphology of the produced electrocatalysts were examined using Carl Zaiss/GeminiSEM 500 field emission scanning electron microscope (FESEM).

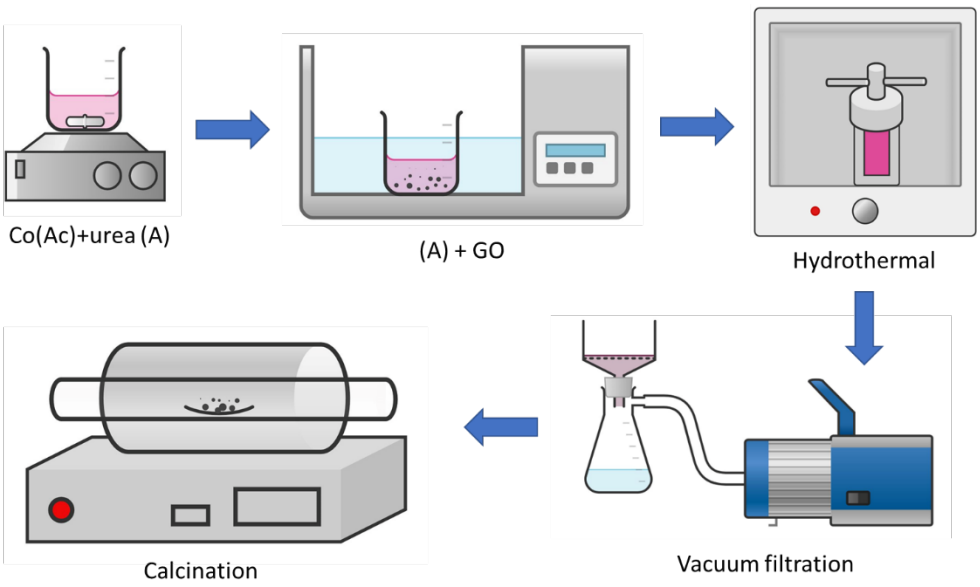

FIGURE 1 Schematic diagram of the synthesis of CNx by using a hydrothermal method with different urea concentrations (x=0, 2-1, 1-1, and 1-2).

ELECTROCHEMICAL CHARACTERIZATION

The electrochemical measurements were conducted using an Autolab PGSTAT128N electrochemical workstation and a rotating ring-disk electrode (RRDE) provided by PINE Instruments. The electrochemical activity was assessed at 25 °C using a standard three-electrode setup. The reference electrode used was Ag/AgCl (3.0 M KCl), while a modified glassy carbon RRDE with a diameter of 5 mm served as the working electrode. Prior to the experiment, the ring-disk electrode underwent polishing and rinsing. To prepare the electrocatalyst ink, the electrocatalyst (4 mg) was mixed with deionized water (225 µL), isopropanol (225 µL), and Nafion (50 µL, 5 wt. %). Prior to usage, the ink was subjected to sonication for a duration of 30 min at room temperature. The ink obtained (10 µL) was applied onto the electrode and allowed to dry prior to testing. A commercial Pt/C electrocatalyst (20 wt. %) was utilized as a reference and subjected to the same technique as the prepared electrocatalysts. Cyclic voltammetry (CV) was conducted using a scan rate of 50 mV s^{-1} in a KOH (0.1 M) saturated with nitrogen gas (N_2) and oxygen gas (O_2). The CV involved a negative scan throughout a potential range of −0.9 to 1.0 V relative to Ag/AgCl, with a platinum wire serving as the counter electrode. Equation (1) demonstrates the conversion of potential into a reversible hydrogen electrode (RHE) (Zhang et al. 2020):

$$E_{RHE} = E_{Ag/AgCl} + 0.059 \times pH + E^{0}_{Ag/AgCl} \quad (1)$$

where $E^{0}_{Ag/AgCl}$ = 0.1976 at a temperature of 25 °C. The electron transfer number (n) of the electrocatalyst for the ORR test was calculated by analyzing the linear sweep voltammetry (LSV) curves at rotating speeds of ranging from 400 to 1600 rpm. The measurements were conducted under N_2– and O_2– saturated environments based on the Koutecky-Levich (K–L) equation, specifically Equation (2) (Sudarsono et al. 2020):

$$\frac{1}{j} = \frac{1}{j_k} + \frac{1}{j_l} = \frac{1}{j_k} + \frac{1}{0.62nFAC_0D_0^{2/3}\nu^{-1/6}\omega^{1/2}} \quad (2)$$

The variables j_k, j_l, and j represent the kinetic current density, diffusion-limiting current density, and measured current density, respectively. The Faraday constant (F) is 96485 C mol^{-1}. The bulk concentration of O_2 in 0.1 M KOH, (C_0) is 1.26 × 10^{-6} mol cm^{-3}. The diffusion coefficient of O_2 in 0.1 M KOH, (D_0) corresponding to 1.93 × 10^{-5} cm^2 s^{-1}. The kinetic viscosity of the electrolyte (ν) is 0.01 cm^2 s^{-1}. Lastly, ω is the rotation speed measured in rpm. The electron transfer number was determined by plotting $\frac{1}{j}$ against $\frac{1}{\omega^{1/2}}$. The hydroxide yield (OOH^- %) was determined by applying Equations (3) and (4), where I_d, I_r, and N are the disk current, ring current, and ring-disk coefficient. Paulus et al. (2001) found that the determination of the collection efficiency or ring-disk coefficient (N) can be influenced by the structure of the porous electrode and its rotation speed. N (0.26) was measured using ring (I_r) and disk current (I_d) in a solution of potassium ferricyanide (10 mM) dissolved in KNO_3 (1 M).

$$n = \frac{4I_d}{I_d + \frac{I_r}{N}} \quad (3)$$

$$\text{Hydroxide yield} = \frac{\frac{I_r}{N}}{I_d + \frac{I_r}{N}} \times 100\% \quad (4)$$

The kinetic parameters for ORR were determined by applying Equation (5) to the RDE data:

$$\eta = a \log j_o - b \log j_k \quad (5)$$

where η is the thermodynamic overpotential; j_k is the kinetic current (mA cm^{-2}); j_o is the exchange current density (mA cm^{-2}); a is a constant; and b is the Tafel slope (mV dec^{-1}).

SINGLE CELL PEMFC EVALUATION

A fuel cell performance test was conducted using a single cell PEMFC. A carbon paper with gas diffusion layer (GDL) with the area of 5 cm^2 was utilized as a substrate for both the anode and cathode. Afterwards, an electrocatalyst ink containing CN1-1 (4 mg cm^{-2}) and Pt/C (0.5 mg cm^{-2}) were applied to the cathode and anode of the substrate using the spray method, respectively. The electrodes were positioned on either side of Nafion 212 membranes using a hot-pressing method at a temperature of 120 °C and a pressure of 30 bar for a duration of 3 min. After purging with N_2 for at least 30 min to eliminate any remaining gas, the fuel cell was tested using H_2 gas (100 mL min^{-1}) at the anode and O_2 gas (200 mL min^{-1}) at the cathode. The evaluation was conducted at 94% relative humidity and atmospheric to maintain adequate hydration of the membrane. The reactants at the anode and cathode were humidified by passing the gas through water in a conical bubbling the gas through water in a conical flask. The cell potential was measured using galvanostatic methods to determine its dependence on current density. The measurements were conducted using Fuel Cell Monitor Pro 4.0, a device manufactured by the H-TEC Education GmbH, Germany. The data was collected at temperatures ranging from 25 °C to 80 °C using Fuel Cell Monitor 3.4 software (H-TEC Education). The single cell was placed inside a temperature-controlled oven (Khind OT 2502) to evaluate the effect of temperature on fuel cell performance. The temperature was monitored using a thermocouple

(HOBO) while the humidity is controlled using humidity sensor (Xiomi) with the probe attached to the cell.

RESULTS AND DISCUSSION

SYNTHESIS AND PHYSICOCHEMICAL CHARACTERIZATION

XRD analysis was used to assess the crystalline characteristics of CNx. Figure 2 displays the spectra of CNx, showing two district diffraction peaks located at 2θ=26.44° and 44.55°. These peaks are attributed to the (002) and (101) planes of a graphitic structure. The peaks seen at 2θ=18.99°, 31.25°, 36.83°, 38.53°, 44.79°, 55.64°, 59.34°, 65.22°, 77.32°, and 78.38° can be attributed to the (111), (022), (113), (222), (004), (224), (115), (044), (335), and (226) crystallographic planes of the cubic spinel-phase structure of Co_3O_4 (ICSD 98-001-5043). The structural characteristics and crystalline phase compositions of the CNx products (Table 1) were determined using Rietveld refinement. The Co_3O_4 patterns fitted using Rietveld method validate the presence of a cubic spinel structure with a Fd-3m space group and equal lattice parameters of a=b=c. The lattice parameter and unit cell volume of Co_3O_4 are consistent with the values documented in the literature (Cardenas-Flechas, Raba & Rincón-Joya 2020). The XRD analysis in Table 1 shows that the crystallite sizes of Co_3O_4 in CNx range from 29 to 48 nm. The crystallite sizes exhibited a steady increase with the rising urea concentration, accompanied by a corresponding increase in the Co_3O_4 crystalline phase composition.

Figure 3 illustrates the FESEM images of CNx products combined with different proportions of urea. The morphologies indicate that the Co_3O_4 were uniformly grown in nanoparticle form, while the GO existed as a 2D sheet, which was prepared to support the Co_3O_4 nanoparticles. The surface morphological images exhibit a homogeneous dispersion of Co_3O_4 particles on both the outer and inner surfaces of GO. The Co_3O_4 particles produced exhibit a broad size distribution, ranging from tens to hundreds of nanometers. The density of Co_3O_4 particles adhered to GO was seen to rise in correlation with the escalating urea content.

Figure 4 displays the Raman spectra of GO and CNx throughout the wavelength range of 100–3000 cm^{-1}. GO displays three distinct vibrational peaks at 1351, 1578, and 2700 cm^{-1}, which correspond to D (defective), G (graphitic), and 2D (second order of D band) bands, respectively. The D band is associated with the vibrational mode of the k-point phonons of A_{1g} symmetry, which suggests the existence of defects or irregularities in the graphitic lattice. The G band corresponds to the E_{2g} phonon of the sp^2 carbon atoms, which represents the stretching vibrations of the graphitic lattice in the plane.

Consequently, the intensity ratio of the D and G bands (I_D/I_G) was computed for CNx to assess the crystal structure's homogeneity, disorder, and defects (Table 2). For CNx, the Raman spectra of the electrocatalysts show the distinctive peaks of Co_3O_4 and GO within the identical range. The Raman spectra of NC0 has vibrational peaks at 1350 and 1578 cm^{-1}, which corresponding to the D and G bands of GO, respectively. Additional vibrational peaks of modest strength emerge at 673, 515, and 470 cm^{-1}, corresponding to A_{1g}, F_{2g}, and E_g modes of Co_3O_4, respectively. These low-intensity peaks were compared with the Raman spectrum of bare GO and verified the presence of the Co_3O_4 crystalline phase in CNx. Additionally, the Raman spectrum shows that the quantity of Co_3O_4 increased with higher urea composition. The obtained outcome is consistent with the significant concentration of Co_3O_4 particles deposited on GO in CNx, as demonstrated by the XRD findings and FESEM morphologies presented in Figures 2 and 3, correspondingly. The increase in Raman intensity of Co_3O_4 modes with increasing urea composition may contribute to a stronger Raman signal, serving as a qualitative indicator of the relative amount of the compound in the samples; however, it does not provide a direct quantitative measure (Saletnik, Saletnik & Puchalski 2021). The FESEM morphology (Figure 3) and XRD Rietveld quantification analysis (Table 1) indicate that the size of nanoparticles and the crystalline phase of Co_3O_4 increased with urea significantly influences the growth of Co_3O_4 nanoparticles.

The intensity ratio (I_D/I_G) of GO was determined to be 1.59. The hydrothermal treatment decreased the I_D/I_G ratio of GO, as indicated by the lower I_D/I_G ratio of CN0 (1.53). While a lower I_D/I_G ratio typically indicates decreased disorder and an increase in the graphitic properties of the carbon material, it does not necessarily imply a significant change in the graphitic structure in this instance (Ferrari 2007). The sample CN2-1 and CN1-1, which incorporated of urea into the reaction system, exhibit I_D/I_G values of 1.55 and 1.60, respectively. These values resemble those of the GO. The observed increase in the I_D/I_G ratio of CN2-1 and CN1-1 suggests that the incorporation of urea might have resulted in the emergence of additional defects or disorder within the graphene structure. The A_{1g}, F_{2g}, and E_g modes of Co_3O_4 may affect the Raman spectrum of the composite material. The Co_3O_4 nanoparticles were mainly deposited or anchored onto GO, leading to a restricted number of active vibrational modes for the GO (Osaimany et al. 2019). Consequently, Co_3O_4 nanoparticles act as a spacer to inhibit the re-stacking of GO (Li & Östling 2013). The limited active vibrational modes for GO in the composite material could also stem from the Co_3O_4 nanoparticles that cover the GO surface, hindering the excitation of the GO lattice vibration. Nonetheless, the comparative intensity ratio of CN1-2 (1.06) is lower than that of CN0, CN2-1, and CN1-1, suggesting a decrease in defect density. The sample CN1-1, prepared with 1:1 molar ratio of $Co(CH_3COO)_2.4H_2O$ to $CO(NH_2)_2$ demonstrates the most significant defect density and electrochemical activity compared to other samples.

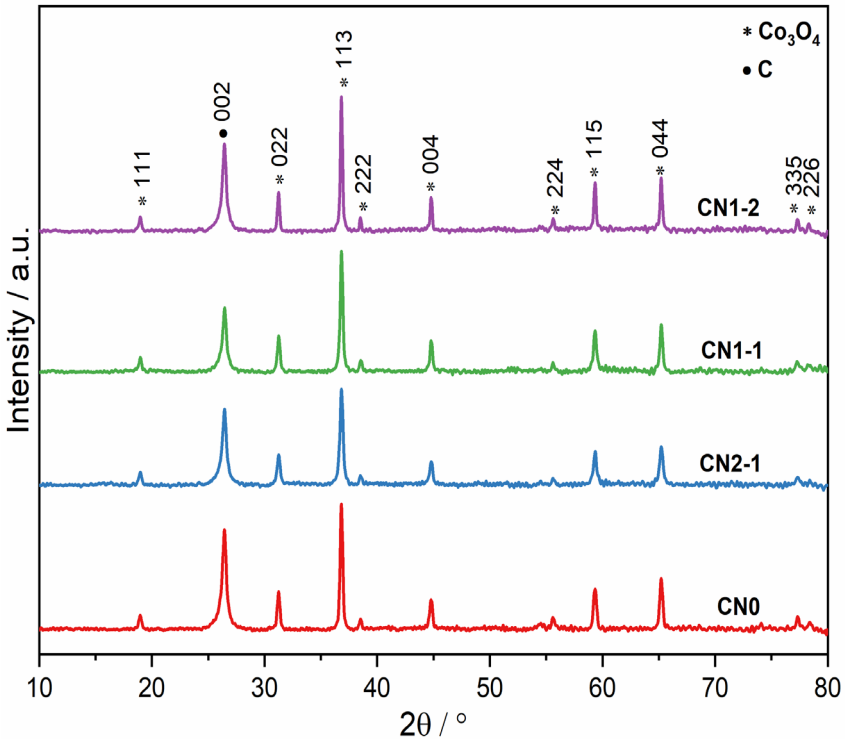

FIGURE 2 XRD spectra of CNx electrocatalysts obtained through a hydrothermal technique.

TABLE 1 Refinement parameters.

Sample	R expected	R profile	Weighted R profile	Goodness of fit	Lattice parameters (Å) a=b=c	Crystallite size (nm)	Micro strain (%)	Crystalline phase (%)	
								Co_3O_4	C
CN0	2.202	1.765	2.216	1.01	8.083	29	0.070	20.6	79.4
CN2-1	2.230	2.006	2.452	0.990	8.083	34	0.101	22.4	77.6
CN1-1	2.177	1.618	2.054	0.980	8.085	37	0.087	23.3	76.7
CN1-2	2.350	1.808	2.245	0.913	8.084	48	0.047	28.8	71.2

TABLE 2 Position and intensity ratios of Raman vibrational bands.

Sample	Position of bands (cm^{-1})			I_D/I_G	I_{2D}/I_G
	D band	G band	2D band		
GO	1351	1578	2700	1.59	0.50
CN0	1350	1578	2717	1.53	0.41
CN2-1	1347	1581	2695	1.55	0.50
CN1-1	1347	1581	2694	1.60	0.50
CN1-2	1353	1581	2700	1.06	0.53

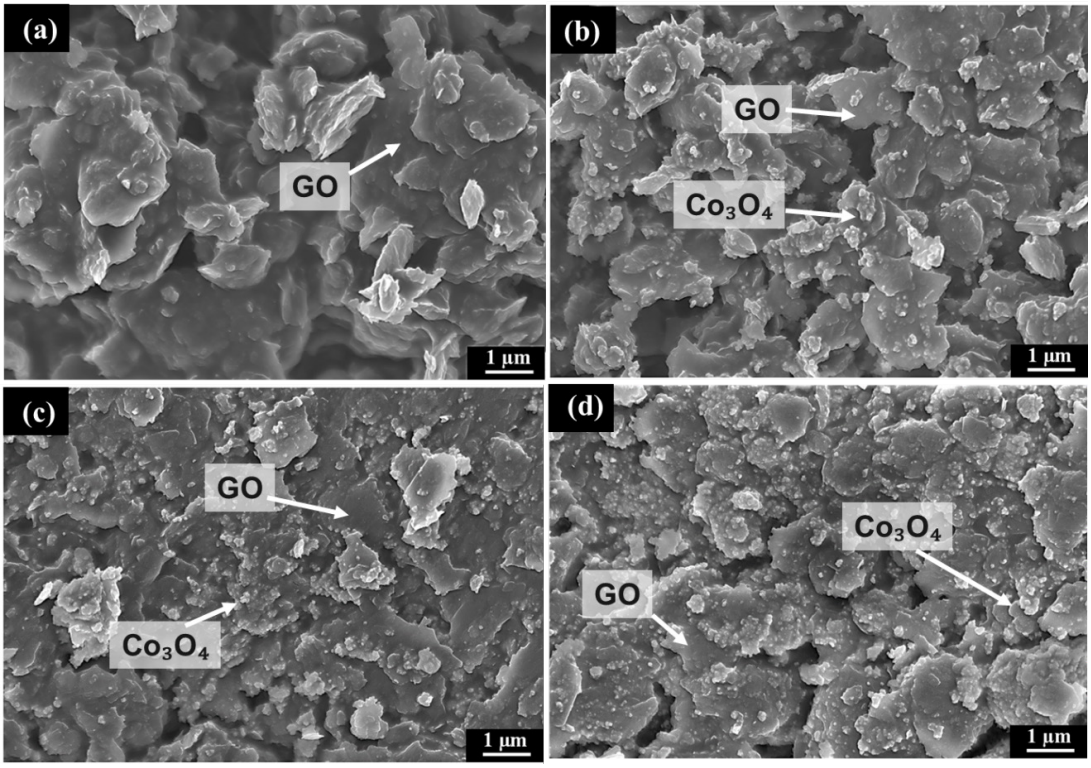

FIGURE 3 FESEM images of GO-supported Co_3O_4 nanoparticles with different urea concentrations: (a) CN0 (b) CN2-1 (c) CN1-1, and (d) CN1-2.

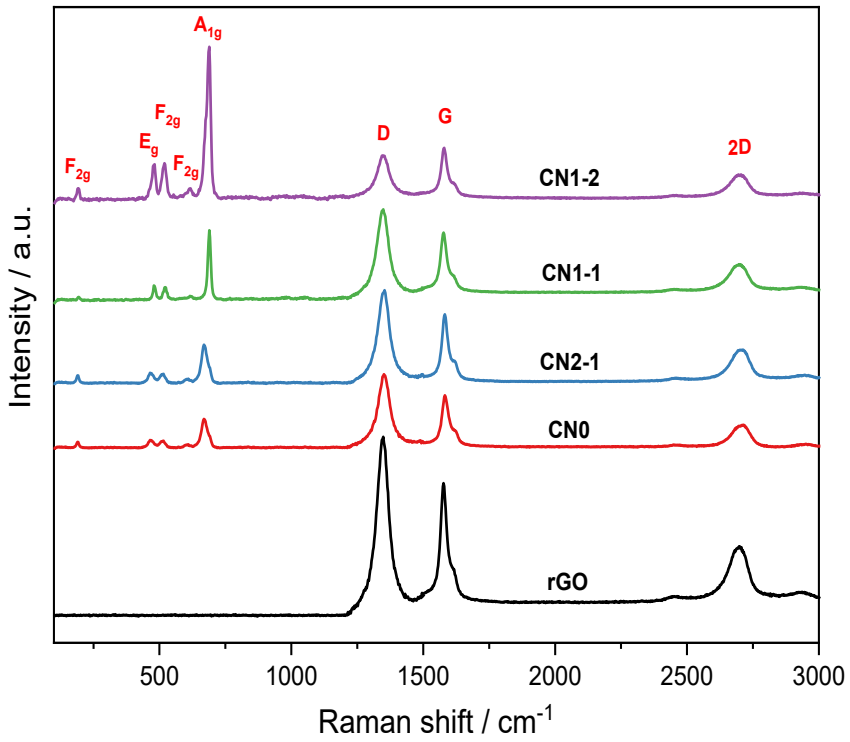

FIGURE 4 Raman spectra of CNx.

ELECTROCHEMICAL CHARACTERIZATION

Figure 5 displays the electrochemical behaviors of CNx and commercial Pt/C in N_2– and O_2– saturated 0.1 M KOH. Figure 5(a) demonstrates that the CN1-1 ORR polarization curves exhibit a distinct and rapid rise in kinetic current density (J_k) in a mixed kinetic zone, which is then followed by a stable plateau of limiting current density (J_l) as the rotation speeds increase. The observed outcome can be ascribed to the fluctuations in the electron transfer, usage of surface-active sites, synergistic impact, and length of ion/electron diffusion path. The polarization curves for CNx were examined at a faster rotating speed of 1600 rpm and compared with 20 wt. % Pt/C to showcase the electrocatalytic capabilities of CNx through the synergetic interplay between Co_3O_4 and GO, as illustrated in Figure 5(b). The onset potentials (E_{onset}) of CN0, CN2-1, CN1-1, and CN1-2 are 0.82, 0.86, 0.88, and 0.86 V, respectively. The half-wave potentials ($E_{1/2}$) for the above samples are 0.65, 0.67, 0.77, and 0.69 V. The diffusion-limited current densities (J_l) measured at 0.4 V are 2.73, 3.86, 4.49, and 3.88 mA cm^{-2}, respectively. CN1-1 exhibits the most favorable E_{onset} and $E_{1/2}$ values, as well as the highest J_L. Nevertheless, in CNx with the greatest urea concentration (CN1-2), the J_L experienced a drop. This could be attributed to the lower defect density and the aggregation of Co_3O_4 nanoparticle over GO, resulting in a reduced quantity of catalytically active sites. Therefore, an optimized CN1-1 composition can result in enhanced electrocatalytic performance. Furthermore, the elevated junctional leakage of CN1-1 near that of the commercially available 20 wt. % Pt/C.

Figure 5(c) illustrated the Tafel slope characteristics, which depict the relationship between the kinetic current density and potential for all the samples. The kinetic current density (J_K) was calculated based on the polarization curves using Equation (2). The Tafel slope values for each sample were determined, and the results indicate the following order: CN1-1=CN1-2 < CN2-1 < CN0. CN1-1 and CN1-2 demonstrate a Tafel slope that is nearly equivalent to that of the commercial Pt/C, indicating a minimal difference. The electron transfer number (n) and hydroxide yield were determined by analyzing the polarization curves obtained from the RRDE (Figure 5(d)) by using Equations (3) and (4). The values of n and OOH^- % are contingent upon the potential of the disc. The n values of CN0, CN2-1, CN1-1, and CN1-2 are 3.78, 3.85, 3.89, and 3.86, respectively. The results indicate that the ORR activity of all samples occurs through a four-electron mechanism. Furthermore, the concentration of OOH^- % of the samples ranges from 5% to 11%. Figure 5(e) displays the K–L plots for CN1-1, illustrating the relationship between inverse current density (j^{-1}) and the inverse square root of the rotation speed ($\omega^{-½}$) within the limited current range of 0.2–0.6 V. The K–L graphs at various electrode potentials exhibit parallelism, indicating the existence of first-order reaction kinetics with respect to the concentration of dissolved oxygen (Sun et al. 2020).

The electrocatalysts' stability was assessed using chronoamperometry at a potential of 0.70 V_{RHE} for both commercial Pt/C and CN1-1. Varying the applied voltage will give a different result, as a higher voltage may lead to an accelerate degradation of the catalyst. At 0.70 V_{RHE} applied voltage, the ORR becomes more prominent in comparison to other competing reactions, such as water electrolysis. This facilitates a more outcome concentrated assessment of the stability of the ORR catalyst. Figure 5(f) demonstrates that the present retention of CN1-1 is 65%, surpassing the 60% retention of commercial Pt/C. The exceptional stability of the electrocatalyst can be ascribed to the robust connection between GO support and the metal oxides. The superior performance of CN1-1 in terms of ORR can be ascribed to the microstructure and composition findings elucidated in the physicochemical characterization. Initially, Co_3O_4 was synthesized in its original location from the precursor, guaranteeing the cooperative impact resulting from the interaction between Co_3O_4 nanoparticles and GO. This interaction enhances the ability to transmit electric charge, which is beneficial for improving reactions at the oxygen electrode. Furthermore, CN1-1 exhibits the most significant defect density compared to the other electrocatalyst, indicating its superior electrochemical activity. Therefore, CN1-1 demonstrates a Tafel slope that is smaller than that of any other samples.

Figure 6 displays the polarization curve, with the x-axis representing the current density, and the primary and secondary y-axes representing potential and power density, respectively. A temperature range of 25 °C to 80 °C was utilized to conduct a single cell performance test, with the objective of determining the highest temperature at which the electrocatalyst can operate. The power density generated at a temperature of 25 °C reaches its lowest value of 22.2 mW cm^{-2} with open circuit potential (OCP) at 0.83 V. This could be attributed to the fact that the operating temperature has not yet reached the activation energy required for cell response. At an elevated working temperature of 60 °C, the maximum power density of 37.9 mW cm^{-2} is achieved due to enhanced reactant transport and kinetics. At an operating temperature of 80 °C, the reaction activity experiences a little reduction to 35.3 mW cm^{-2}. These findings indicate that the temperature induced deterioration of the electrocatalyst's active site, resulting in a reduction at the rate of mass transfer. However, the OCV for all temperature ranges is much below the expected value of 0.9–1.2 V for Pt/C. The observed result may be attributed to the significant parasitic current generated by electrical shorts or fuel cross-over (Seeberger et al. 2020). Meanwhile, the measured power density of the single cell is seemed smaller compared to Pt/C (173.6 mW cm^{-2}) as shown in Figure 6(b). With further optimization, including adjustments to electrocatalyst loading, membrane electrode assembly (MEA) preparation parameters, and fuel flow rate, the performance of PEMFC is expected to improve, making it a more viable alternative to Pt/C.

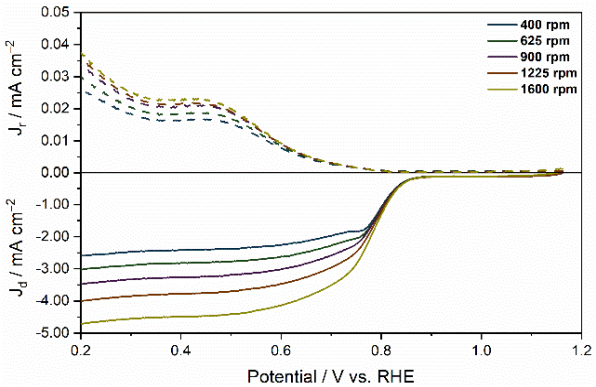

(a)

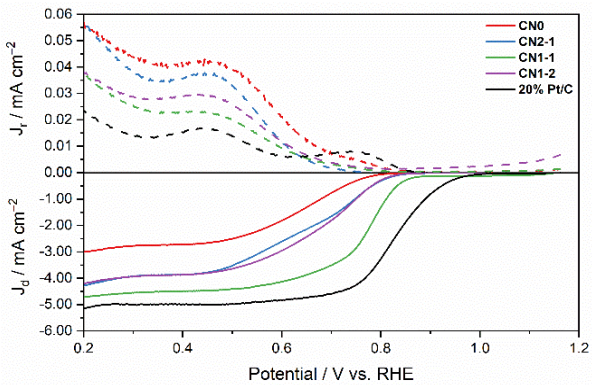

(b)

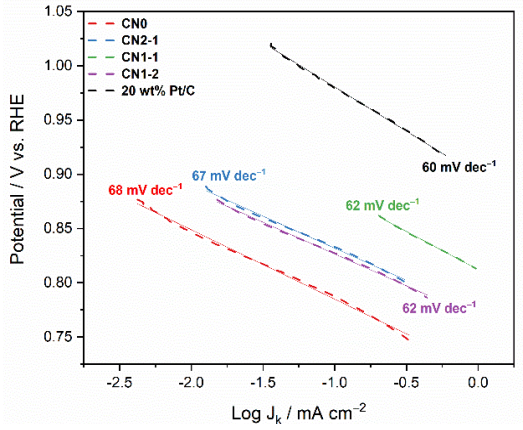

(c)

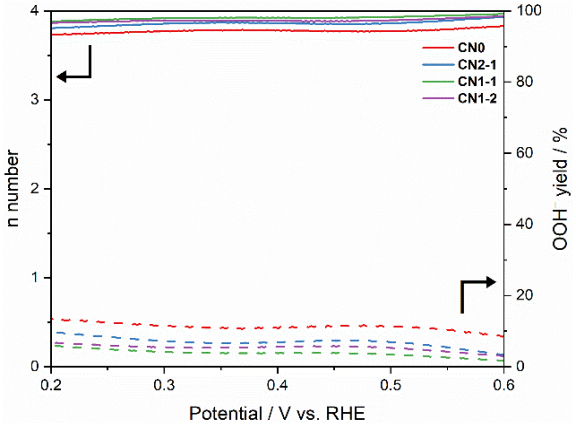

(d)

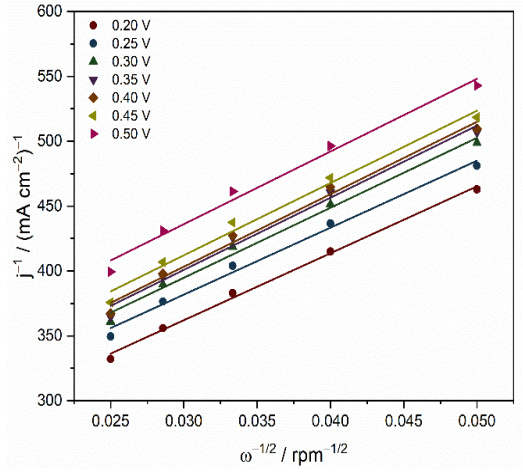

(e)

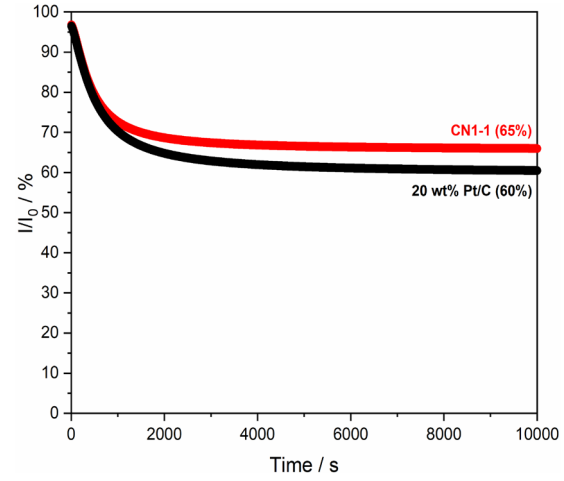

(f)

FIGURE 5 (a) ORR polarization curves of CN1-1 under various rotation rates, (b) LSV curves of CNx with different urea concentrations, (c) derived Tafel plots from the corresponding ORR curves in the kinetic current density region, (d) number of electrons (n) and production of peroxide for CNx, (e) corresponding K–L plots for CN1-1, and (f) stability tests of CN1-1 and commercial Pt/C at 0.7 V_{RHE} in O_2–saturated 0.1 M KOH.

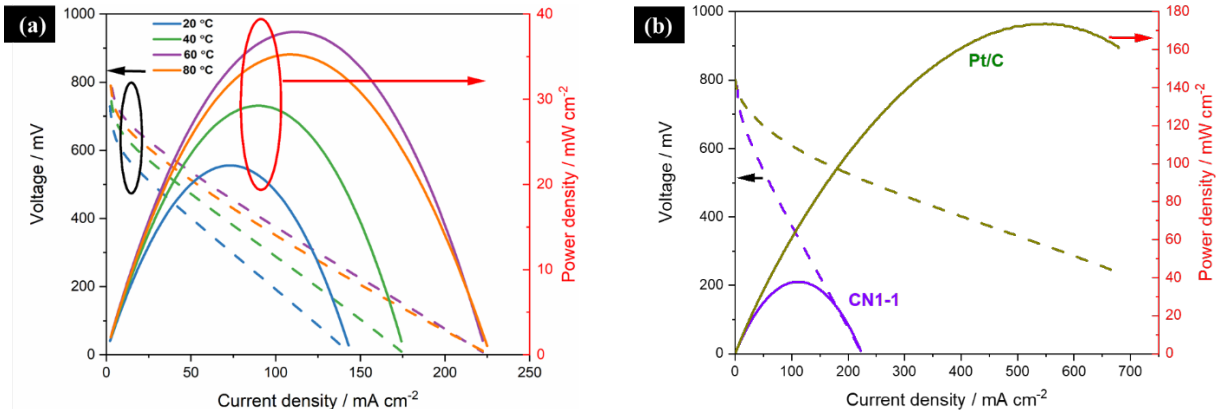

FIGURE 6 Polarization curves and power densities under O_2 (200 mL min^{-1}) and H_2 (100 mL min^{-1}) 94% RH of (a) CN1-1 tested from 25 °C to 80 °C and (b) CN1-1 and Pt/C at 60 °C.

CONCLUSIONS

Co_3O_4 nanoparticles were produced on GO support using different doses of urea via a hydrothermal method, followed by calcination. The Co_3O_4 nanoparticles have been evenly distributed on the surface of the GO. The quantity of urea employed in the reaction system exerts a substantial impact on electrocatalytic activity. The CN1-1 sample, made with a 1:1 ratio of $Co(CH_3COO)_2.4H_2O$ to $CO(NH_2)_2$ has improved ORR performance. It exhibits a higher onset potential of 0.88 V, larger diffusion limiting current density of 4.49 mA cm^{-2}, and a faster reaction rate with a slope of 62 mV dec^{-1}. These enhancements are attributed to a four-electron transfer mechanism (n=3.89). According to the procedure for setting up the half-cell, the CN1-1 that was produced exhibits more stability compared to Pt/C. Subsequently, a single fuel cell was fabricated utilizing CN1-1 as cathode electrode, yielding a power density of 37.9 mW cm^{-2} at 60 °C. Nevertheless, the electrocatalyst optimized with cobalt acetate tetrahydrate and urea in a 1:1 ratio (CN1-1) shows potential as a viable substitute of Pt/C commercial ORR electrocatalysts in fuel cell applications. Hence, it is imperative to perform more extensive research utilizing the synthesized electrocatalyst to enhance the electrode formulation and MEA conducted using the synthesized electrocatalyst to optimize the electrode formulation and MEA fabrication for practical cell operation.

ACKNOWLEDGMENTS

The authors gratefully acknowledge the financial support from Universiti Kebangsaan Malaysia under grants No. GUP-2023-037 and PP-SELFUEL-2024 and the International Atomic Energy Agency for grant under Coordinated Research Project (IAEA-CRP-R23130).

REFERENCES

Basri, S., Hazri, N.S., Selladurai, S.R., Zainoodin, A.M., Kamarudin, S.K., Zakaria, S.U. & Hashim, A.R. 2020. Analysis of $Mg(OH)_2$ deposition for magnesium air fuel cell (MAFC) by saline water. *Sains Malaysiana* 49(12): 3105-3115.

Cardenas-Flechas, L.J., Raba, A.M. & Rincón-Joya, M. 2020. Synthesis and evaluation of nickel doped Co_3O_4 produced through hydrothermal technique. *DYNA (Colombia)* 87(213): 184-191.

Chandrasekaran, S., Ma, D., Ge, Y., Deng, L., Bowen, C., Roscow, J., Zhang, Y., Lin, Z., Misra, R.D.K., Li, J., Zhang, P. & Zhang, H. 2020. Electronic structure engineering on two-dimensional (2D) electrocatalytic materials for oxygen reduction, oxygen evolution, and hydrogen evolution reactions. *Nano Energy* 77: 105080.

Choi, H.J., Ashok Kumar, N. & Baek, J.B. 2015. Graphene supported non-precious metal-macrocycle catalysts for oxygen reduction reaction in fuel cells. *Nanoscale* 7(16): 6991-6998.

Ferrari, A.C. 2007. Raman spectroscopy of graphene and graphite: Disorder, electron-phonon coupling, doping and nonadiabatic effects. *Solid State Communications* 143(1-2): 47-57.

Gebremariam, T.T., Chen, F., Wang, Q., Wang, J., Liu, Y., Wang, X. & Qaseem, A. 2018. Bimetallic Mn-Co oxide nanoparticles anchored on carbon nanofibers wrapped in nitrogen-doped carbon for application in Zn-air batteries and supercapacitors. *ACS Applied Energy Materials* 1(4): 1612-1625.

He, H., Feng, Y., Wang, H., Wang, B., Xie, W., Chen, S., Lu, Q., Feng, Y. & Xue, L. 2022. Waste-based hydrothermal carbonization aqueous phase substitutes urea for rice paddy return: Improved soil fertility and grain yield. *Journal of Cleaner Production* 344: 131135.

Ji, Z., Perez-Page, M., Chen, J., Rodriguez, R.G., Cai, R., Haigh, S.J. & Holmes, S.M. 2021. A structured catalyst support combining electrochemically exfoliated graphene oxide and carbon black for enhanced performance and durability in low-temperature hydrogen fuel cells. *Energy* 226: 120318.

Kaewsai, D., Yeamdee, S., Supajaroon, S. & Hunsom, M. 2018. ORR activity and stability of PtCr/C catalysts in a low temperature/pressure PEM fuel cell: Effect of heat treatment temperature. *International Journal of Hydrogen Energy* 43(10): 5133-5144.

Khan, I.A., Qian, Y., Badshah, A., Nadeem, M.A. & Zhao, D. 2016. Highly porous carbon derived from MOF-5 as a support of ORR electrocatalysts for fuel cells. *ACS Applied Materials and Interfaces* 8(27): 17268-17275.

Lai, X., Liu, C., He, H., Li, J., Wang, L., Long, Q., Zhang, P. & Huang, Y. 2020. Hydrothermal synthesis and characterization of nitrogen-doped fluorescent carbon quantum dots from citric acid and urea. *Ferroelectrics* 566(1): 116-123.

Li, J. & Östling, M. 2013. Prevention of graphene restacking for performance boost of supercapacitors-a review. *Crystals 3*(1): 163-190.

Olabi, A.G., Sayed, E.T., Wilberforce, T., Jamal, A., Alami, A.H., Elsaid, K., Mohammod, S., Rahman, A. & Shah, S.K. 2021. Metal-air batteries - A review. *Energies* 14(21): 7373.

Osaimany, P., Samuel, A.S., Johnbosco, Y., Kharwar, Y.P. & Chakravarthy, V. 2019. A study of synergistic effect on oxygen reduction activity and capacitive performance of $NiCo_2O_4$/rGO hybrid catalyst for rechargeable metal-air batteries and supercapacitor applications. *Composites Part B: Engineering* 176: 107327.

Paulus, U.A., Schmidt, T.J., Gasteiger, H.A. & Behm, R.J. 2001. Oxygen reduction on a high-surface area Pt/Vulcan carbon catalyst: A thin-film rotating ring-disk electrode study. *Journal of Electroanalytical Chemistry* 495(2): 134-145.

Rahman, K.R., Kok, K.Y., Wong, W.Y., Yang, H. & Lim, K.L. 2021. Effect of iron loading on the catalytic activity of Fe/N-doped reduced graphene oxide catalysts via irradiation. *Applied Sciences* 11(1): 205.

Roudbari, M.N., Ojani, R. & Raoof, J.B. 2020. Nitrogen functionalized carbon nanotubes as a support of platinum electrocatalysts for performance improvement of ORR using fuel cell cathodic half-cell. *Renewable Energy* 159: 1015-1028.

Saidin, N.U., Choo, T.F., Mohamad Yunus, R., Mat Zali, N., Kok, K.Y., Wong, W.Y. & Lim, K.L. 2023. One-pot gamma radiolysis synthesis of a graphene oxide-supported cobalt oxyhydroxide electrocatalyst for oxygen reduction reaction. *Radiation Physics and Chemistry* 205: 110680.

Saletnik, A., Saletnik, B. & Puchalski, C. 2021. Overview of popular techniques of Raman spectroscopy and their potential in the study of plant tissues. *Molecules* 26(6): 1537.

Seeberger, D., McLaughlin, D., Hauenstein, P. & Thiele, S. 2020. Bipolar-interface fuel cells - an underestimated membrane electrode assembly concept for PGM-free ORR catalysts. *Sustainable Energy and Fuels* 4(5): 2508-2518.

Shahid, M.M., Zhan, Y., Alizadeh, M., Sagadevan, S., Paiman, S. & Oh, W.C. 2020. A glassy carbon electrode modified with tailored nanostructures of cobalt oxide for oxygen reduction reaction. *International Journal of Hydrogen Energy* 45(38): 18850-18858.

Sudarsono, W., Wong, W.Y., Loh, K.S., Majlan, E.H., Syarif, N., Kok, K.Y., Yunus, R.M. & Lim, K.L. 2020. Noble-free oxygen reduction reaction catalyst supported on Sengon wood (*Paraserianthes falcataria* L.) derived reduced graphene oxide for fuel cell application. *International Journal of Energy Research* 44(3): 1761-1774.

Sun, C., Alonso, J.A. & Bian, J. 2021. Recent advances in perovskite-type oxides for energy conversion and storage applications. *Advanced Energy Materials* 11(2): 2000459.

Sun, J., Yang, Y., Wang, J., Zhang, Z. & Guo, J. 2020. *In-situ* construction of cobalt oxide/ nitrogen-doped porous carbon compounds as efficient bifunctional catalysts for oxygen electrode reactions. *Journal of Alloys and Compounds* 827: 154308.

Tashie-Lewis, B.C. & Nnabuife, S.G. 2021. Hydrogen production, distribution, storage and power conversion in a hydrogen economy - A technology review. *Chemical Engineering Journal Advances* 8: 100172.

Tellez-Cruz, M.M., Escorihuela, J., Solorza-Feria, O. & Compañ, V. 2021. Proton exchange membrane fuel cells (PEMFCs): Advances and challenges. *Polymers* 13(18): 3064.

Wan Mansor, W.N., Abdullah, S., Che Wan Othman, C.W.M.N., Jarkoni, M.N.K., Chao, H.R. & Lin, S.L. 2020. Data on greenhouse gases emission of fuels in power plants in Malaysia during the year of 1990-2017. *Data in Brief* 30: 105440.

Wang, K.X., Zhu, Q.C. & Chen, J.S. 2018. Strategies toward high-performance cathode materials for lithium–oxygen batteries. *Small* 14(27): 1800078.

Yang, H., Ko, Y., Lee, W., Züttel, A. & Kim, W. 2019a. Nitrogen-doped carbon black supported Pt–M (M = Pd, Fe, Ni) alloy catalysts for oxygen reduction reaction in proton exchange membrane fuel cell. *Materials Today Energy* 13: 374-381.

Yang, H., Zhu, M., Guo, X., Yan, C. & Lin, S. 2019b. Anchoring $MnCo_2O_4$ nanorods from bimetal-organic framework on rGO for high-performance oxygen evolution and reduction reaction. *ACS Omega* 4(27): 22325-22331.

Ye, H., Li, L., Liu, D., Fu, Q., Zhang, F., Dai, P., Gu, X. & Zhao, X. 2020. Sustained-release method for the directed synthesis of ZIF-derived ultrafine Co-N-C ORR catalysts with embedded Co quantum dots. *ACS Applied Materials and Interfaces* 12(52): 57847-57858.

Yusoff, F. & Suresh, K. 2021. Performance of reduced graphene oxide/iron(III) oxide/silica dioxide ($rGO/Fe_3O_4/SiO_2$) as a potential oxygen reduction electrocatalyst in fuel cell. *Sains Malaysiana* 50(7): 2017-2024.

Zakaria, Z., Kamarudin, S.K. & Wahid, K.A.A. 2021. Fuel cells as an advanced alternative energy source for the residential sector applications in Malaysia. *International Journal of Energy Research* 45(4): 5032-5057.

Zhang, Y., Shi, J., Huang, Z., Guan, X., Zong, S., Cheng, C., Zheng, B. & Guo, L. 2020. Synchronous construction of CoS_2 *in-situ* loading and S doping for g-C3N4: Enhanced photocatalytic H_2-evolution activity and mechanism insight. *Chemical Engineering Journal* 401: 126135.

Zhao, H., Xing, T., Li, L., Geng, X., Guo, K., Sun, C., Zhou, W., Yang, H., Song, R. & An, B. 2019. Synthesis of cobalt and nitrogen co-doped carbon nanotubes and its ORR activity as the catalyst used in hydrogen fuel cells. *International Journal of Hydrogen Energy* 44(46): 25180-25187.

Zhu, Z., Yin, H., Wang, Y., Chuang, C.H., Xing, L., Dong, M., Lu, Y.R., Casillas-Garcia, G., Zheng, Y., Chen, S., Dou, Y., Liu, P., Cheng, Q. & Zhao, H. 2020. Coexisting single-atomic Fe and Ni sites on hierarchically ordered porous carbon as a highly efficient ORR electrocatalyst. *Advanced Materials* 32(42): 2004670.

*Corresponding author; email: shahbud@ukm.edu.my